Assessing the localization, stability, and recovery of inorganic nanoparticles in tree bark using advanced degradation techniques

Sophie Coural, Mickaël Tharaud, Bérénice Piquet, Perrine Chaurand, Marc F Benedetti, Yann Sivry

Journal of Hazardous Materials 506 (2026) 141584

Contents lists available at ScienceDirect

Journal of Hazardous Materials

journal homepage: www.elsevier.com/locate/jhazmat

Assessing the localization, stability, and recovery of inorganic nanoparticles in tree bark using advanced degradation techniques

Sophie Coural [a], Mickaël Tharaud [a], Bérénice Piquet [b], Perrine Chaurand [c], Marc F. Benedetti [a], Yann Sivry [a,*]

[a] Université Paris Cité, Institut de physique du globe de Paris, CNRS, Paris F-75005, France
[b] Electron Microscopy Platform, Muséum National d'Histoire Naturelle, UMR 7245 MCAM MNHN-CNRS, Muséum National d'Histoire Naturelle, Paris, France
[c] Aix Marseille Univ., CNRS, IRD, INRAE, Coll. France, CEREGE, Aix-en-Provence, France

HIGHLIGHTS

- Metallic NPs are localized at bark surface and in porous inner structures
- First application of cold O_2 plasma and TMAH digestion to tree bark
- O_2 plasma achieves 89 % degradation and preserve selectively oxide NPs
- Impact of degradation strategy on nanoparticle preservation is evaluated

GRAPHICAL ABSTRACT

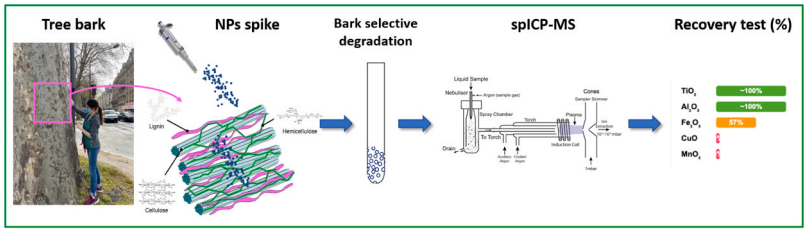

ARTICLE INFO

Keywords:
Atmospheric nanoparticles
Tree barks bioindicators
Organic matter degradation
Nanoparticle stability
Degradation techniques
spICP-MS

ABSTRACT

This study presents methodological advancements for characterizing atmospheric nanoparticles (NPs) accumulated in tree bark, a passive bioindicator of urban nanoparticle pollution. Accurate assessment requires efficient degradation methods that remove organic matter while preserving inorganic NP properties. Preliminary imaging (SEM, X-ray microtomography) and chemical mapping revealed heterogeneous NP distributions, with preferential accumulation at the bark surface and partial penetration into internal porous structures. Two degradation strategies – tetramethylammonium hydroxide (TMAH) digestion and cold O_2 plasma treatment – were evaluated using bark doped with engineered NPs (Au, Fe_2O_3, MnO_2, TiO_2, Al_2O_3, CuO) at environmentally relevant concentrations. TMAH removed 27 % of bark dry weight, while O_2 plasma achieved 89 %, confirmed by FTIR analysis showing disappearance of lignin and cellulose peaks. spICP-MS quantification demonstrated that O_2 plasma preserved TiO_2 and Al_2O_3 (~100 % recovery), partially degraded Fe_2O_3 (-43 % mass loss), and fully degraded CuO and MnO_2, likely due to ionization energy thresholds and oxidation state transitions. TMAH induced partial Fe_2O_3 dissolution and CuO aggregation via complexation and electrostatic interactions. These results highlight the critical influence of degradation protocols on NP stability and underscore the need for optimized methods that efficiently remove organic matter while maintaining NP integrity. This work provides a robust analytical framework for environmentally relevant studies of nanoparticle behavior, persistence, and potential hazard in complex biological matrices.

* Corresponding author.
E-mail address: sivry@ipgp.fr (Y. Sivry).

https://doi.org/10.1016/j.jhazmat.2026.141584
Received 28 November 2025; Received in revised form 26 January 2026; Accepted 21 February 2026
Available online 22 February 2026

1. Introduction

Nanoparticles (NPs, $1 \leq$ size ≤ 100 nm) are raising growing concerns about their potential impact on human health and the environment, with fluxes of the order of Tg/year, varying according to their source. The flow of incidental anthropogenic NPs is in the order of 1–10 Tg/year and can contribute to air, soil and river pollution [1]. Inorganic particles released in the urban atmosphere are metallic oxides particles such as Fe_3O_4, but also TiO_2, MnO_2 and CuO, which come from traffic activities such as exhaust emissions, brake pad wear and tire abrasion [2,3]. In addition, particles are also produced by other sources of activity such as industrial, residential combustion [4] and the erosion of buildings [5].

In the environment, they can disperse and accumulate in soil and water, potentially affecting ecosystems and food chains. Metallic NPs can disrupt the growth of plants and micro-organisms, which are essential to biodiversity [6]. Several studies on the impact of atmospheric NPs on human health have been conducted and because of their size, they can easily penetrate living organisms, crossing biological barriers and reaching organs such as the lungs, brain and liver. Once in the body, they can generate oxidative stress, a chemical reaction that damages cells and tissues [7] and epidemiological studies show that exposure to air pollution NPs increases the risk of cardiovascular disease, including stress and systemic pulmonary inflammation, nervous system imbalances [8,9]. The risk therefore depends on parameters like the chemical composition, number and size distribution of these particles. Even though the danger is recognized, the human health risk assessment also requires characterizing the exposure of the general population to atmospheric NPs.

In urban areas, various methods are used to measure ultrafine particle concentrations and distributions. Condensation Particle Counters (CPCs) allow for real-time measurements of particle number concentration, while Scanning Mobility Particle Sizers (SMPSs) provide detailed size, number, and volume distributions of NPs [10]. However, these techniques do not directly determine the chemical composition of the particles, which requires filter-based sampling followed by laboratory analysis using methods such as bulk or LA-ICP-MS [11].

Other methods like field flow fractionation (FFF) or Dynamic light scattering (DLS) can be used to determine the size distribution of NPs [12–14]. X-ray energy dispersive analysis (EDX) combined with scanning electron microscopy (SEM) offers insights into the size and elemental composition of NPs [15] within the range from nano to micron scales. These latter are however limited in that they do not simultaneously provide information directly relevant to assessing potential health impacts. From the past two decades, single-particle inductively coupled plasma-mass spectrometry (spICP-MS) have been developed. It is a technique that can determine elemental composition, particle mass distribution and particle number concentration of suspended NPs in an aqueous solution [16]. It has been used especially to determine the behaviour and fate of NPs surface waters [17–19], with ICP-ToF-MS applied for ash deposits [20] and also in urban area for NPs from road dust leachate [21]. These leachates have been shown to contain trace metal(loid)-bearing NPs originating from atmospheric deposition, vehicular abrasion, and resuspension processes.

High-resolution mapping of atmospheric particle exposure requires a large number of sampling points. However, effectively mapping the exposure spatially, at the scale of a city for instance, remains a significant challenge. These measurements are currently confined to laboratory settings and have not been integrated into air quality monitoring practices. The primary challenge lies in the fact that, although spICP-MS can simultaneously provide size distribution and chemical composition data at the nano-scale, it remains underutilized for generating spatially-resolved maps of atmospheric NPs.

For this purpose, the use of passive biosensors such as tree bark as an indicator of the amount of NPs air pollution can be interesting [22,23]. Some studies already show the presence of metallic particle within the tree bark. Most of these studies usually analyzed the total metallic contents by ICP-MS after full mineralization of the barks, combined with SEM observations of particles [24]. Since the 2000s, analyses have most often focused on heavy metals in urban and industrial areas. In Serbia increased levels of zinc, copper, and lead were observed near busy roads, demonstrating a direct correlation with traffic intensity [25]. Similar results were reported in Nigeria, where the analysis of heavy metals in *Terminalia catapa* bark from parking areas with varying vehicle density revealed a clear link between metal concentrations and both urbanization and vehicle emissions [26].

Plane trees renew their bark once a year, which is why they have recently attracted the interest of scientific studies, mainly using environmental magnetism [27,28]. These studies have focused on total metal measurements, which lack size and number information, and on magnetism, which only captures a fraction of NPs present in bark.

It is therefore paramount to identifying and quantifying the elemental composition of NPs deposited on tree bark to create detailed maps that show where concentrations of different metallic NPs are highest within urban areas, helping to identify pollution hotspots using advanced analytical techniques like spICP-MS. It would be possible to characterize exposure to NPs by combining the use of passive biological bio-indicators, which are widely available in urban areas, with a unique technique giving access to the chemical composition and size distribution of the particles. spICP-MS measurement requires NPs to be suspended in an aqueous phase, which means to transfer inorganic NPs from the tree bark to an aqueous solution. The main chemical components of bark are cellulose, lignin, hemicellulose and suber [29]. From these, lignin binds the bark cells together, providing bark mechanical strength and rigidity to resist external forces. Lignin is an irregular, cross-linked polymer network, which is composed of randomly cross-linked phenylpropanoid units. Hence, tree bark, also called "lignocellulosic material" is a complex and tough organic matrix to degrade. Before selecting a suitable degradation strategy, it is essential to understand how atmospheric NPs are distributed within the bark matrix. In this context, microscopy techniques such as scanning electron microscopy (SEM) and particle-induced X-ray emission (PIXE) have been used [30] to explore element localization within the bark, revealing that some atmospheric contaminants can penetrate beyond the surface and accumulate in specific internal layers. However, such approaches remain limited and have not been routinely applied to the study of NPs.

Given the structural complexity of bark and the potential embedding of inorganic particles in lignified tissues, a controlled degradation of the lignocellulosic matrix is necessary to release the NPs without altering their composition. Advanced Oxidation Processes (AOPs), such as Fenton or Fenton-like reactions, rely on the generation of highly reactive radical species and are primarily designed for the mineralization of low-molecular-weight organic contaminants dissolved in aqueous media, particularly in wastewater treatment [31,32]. However, their application to solid, highly recalcitrant biopolymers such as lignin and cellulose remains limited due to restricted radical accessibility and the intrinsic resistance of these polymeric structures to non-selective oxidative attack.

For biological tissues (e.g., fish and beef tissue), alkaline degradation methods are commonly used, particularly those involving tetramethylammonium hydroxide (TMAH) [33–35]. TMAH digestion at 90 °C for 3 h has been shown to achieve complete solubilization, enabling subsequent chemical and elemental analyses [33]. Efficient solubilization of proteins, amino acids, and lipids in chicken tissue has also been demonstrated using a TMAH-based method, with recovery rates of 90–95 % [34]. However, TMAH has never been tried to degrade bark samples so far. O_2 plasma degradation has been successfully applied to degrade organic matter of various compositions, particularly in refractory plant matrices [36]. This method effectively decomposes cellulose surfaces by breaking polymer chains and forming highly functionalized molecules [36]. This method has been used in fields such as archaeological conservation [37] and biomass processing [38], but its

application to tree bark degradation remains unexplored. In contrast to conventional AOPs, both cold O_2 plasma and alkaline TMAH digestion offer promising alternative degradation strategies better suited for controlled solubilization of complex solid matrices.

Despite the extensive research on these degradation methods, none have simultaneously evaluated their efficiency in degrading tree bark while assessing their impact on NPs. Given that tree bark is both chemically complex and a key bioindicator for environmental pollution, developing an optimized degradation method that preserves nanoparticle properties while efficiently removing organic matter is crucial for accurate environmental assessments.

The objective of this study is thus twofold: (i) to demonstrate the spatial localization of NPs in bark tissue, and (ii) to assess the ability of two methods to selectively degrade the bark while preserving the inorganic particles. The first part focuses on locating metallic NPs within the bark matrix using a combination of complementary and multi-scale techniques: X-ray microtomography for 3D imaging of the internal structure at the micro-scale coupled with thin-sectioning and electron imaging for 2D imaging at higher spatial resolution. In the second part, O_2 cold plasma and TMAH degradation were investigated for the first time in the context of bark matrix degradation, for their ability to release NPs from the bark while preserving their physicochemical characteristics, in order to optimize bark-based environmental monitoring protocols. The degradation efficiency of TMAH and oxygen plasma was first assessed using UV–VIS spectroscopy and FTIR. Then, to evaluate the potential of each method to preserve nanoparticle characteristics during digestion, bark samples were doped at environmentally relevant concentrations with engineered NPs (Au, Fe_2O_3, MnO_2, TiO_2, Al_2O_3, CuO), and the recovery rates and mass distributions of these particles were measured before and after digestion using spICP-MS.

2. Material and methods

2.1. Bark sample

In order to obtain robust recovery calculation during NPs doping tests, it was compulsory to work with a sample as uncontaminated as possible. Therefore, the location chosen for sampling was a forest environment free of NPs from anthropogenic origin. The tree bark from *Platanus sp*. used in this study has been sampled in March of the year 2019 in the Fontainebleau forest (48° 25′ 52.36″ N, 2° 37′ 38.76″ E, Fontainebleau, France). The sampling protocol consisted in detaching several fragments of the bark from the tree at heights between 1 and 1.7 m aboveground, using a plastic bag turned inside out for subsequent storage. The fragments are then stored in the freezer and ground using a grinder (®Mockmill 200) with ceramic blades to avoid metallic contamination. For the particle localization step, two *Platanus sp*. bark samples from Paris were selected based on their high iron content (1189 ppm and 1180 ppm, respectively), compared to only 57 ppm in the Fontainebleau reference bark.

These "contaminated" samples were used to investigate the spatial distribution of naturally accumulated NPs within bark tissues.

2.2. Electron microscopy

Scanning Electron Microscopy (SEM) analyses were performed at IPGP's platform PARI using an Auriga 40 instrument equipped with a Bruker Quantax 200 energy dispersive X-ray spectrometer (EDS), operated at a resolution of 1 nm with an energy beam of 30 keV. To improve noise reduction, the surface of the sample was gold-coated. SmartSEM software was utilized for image acquisition and enhancement.

Transmission Electron Microscopy (TEM) analyses were carried out at the PICMO platform of Université Paris Cité using a Jeol JEM 2100 microscope (LaB6 filament), with a beam energy of 100 kV and a spatial resolution of 0.2 nm.

2.3. 3D imaging by X-ray micro-tomography

X-ray computed-tomography analyses at the micro-scale (micro-CT) were conducted at CEREGE's MATRIX platform using a Zeiss MicroXCT-400 system. Samples were placed in Kapton tubes external face up. Scans were acquired at 40 kV and 250 μA; a total of 2 500 projections were collected through 360° sample rotation with an exposure time of 12 s per projection, resulting in a total acquisition time of 10 h. A 20x magnification optical objective was used to achieve an isotropic voxel of 1 μm and a field of view of 1x1x1 mm^3. Volume reconstruction was performed with XM Reconstructed-Parallel Beam-9.0.6445 software using a filtered back projection algorithm. The brightest voxels, i.e. with highest X-ray absorption, reveal the distribution of metallic particles within the bark matrix, exhibiting lower X-ray absorption. The detail detectability is assumed to be at least 3 times larger than the voxel size (>3 μm).

2.4. Transverse thin sections of tree bark

Bark samples were embedded in a polymerizable resin to stabilize their porous structure and prevent deformation or particle loss during preparation. The embedding process involved several steps: fixation in 2.5 % glutaraldehyde solution in 0.05 M phosphate buffer (pH 7.2) at atmospheric pressure for 24 h, followed by dehydration through a graded series of ethanol and acetone baths. Final resin impregnation was carried out under vacuum using Spurr's resin medium viscosity (EMS).

Once polymerized, thin sections of 150 nm and 500 nm were cut using an ultramicrotome (RMC power tome XL) equipped with a diamond knife (Diatome), and stained with 1 % toluidine blue and 1 % borax to enhance visualization of the cellular structures by SEM and TEM.

2.5. Lignocellulosic material degradation protocol

2.5.1. Tetramethylammonium hydroxide (TMAH)

A 25 wt% laboratory-grade TMAH solution was obtained from Sigma Aldrich®. MQ water (18.2 MΩ cm) was used throughout. An aliquot of 30 mg of bark was mixed with a 10 mL 20 %V/V TMAH aqueous solution. The bark-to-solution ratio was selected based on values commonly used in TMAH digestion protocols reported in the literature (typically 5–25 % v/v) [35]. Preliminary tests conducted using ratios ranging from 10 % to 30 % (v/v) did not show any significant influence on organic matter solubilization; therefore, the selected ratio was retained for all experiments. The samples were sonicated for 20 min and stirred at 80 rpm for 3 days.

2.5.2. O_2 plasma reactor

The samples were digested by an RF Plasma Barrel Etcher PT7160 (Polaron). A cold oxygen plasma reactor works by introducing an oxygen plasma into a chamber where the sample is placed. Oxygen ions and radicals oxidize refractory organic matter, reducing it to simpler compounds such as carbon dioxide and water. This process takes place at a relatively low temperature, between 60°C and 90°C, preventing thermal modification of the metallic NPs. An aliquot of 80 mg bark powder is placed in a ceramic crucible with a Teflon pierced lid. A carrier gas (O_2) is introduced into the chamber, raising the chamber pressure to 0.5 bar. Then a 13.5 MHz radio frequency power is applied around the chamber The sample is digested for 5 h. After degradation, 1 mL of MQ is added and the samples is sonicated for 20 min to remove material from the crucible. Then 9 mL of MQ is added and the solution is transferred in a 15 mL culture tube.

2.6. Lignocellulosic material degradation monitoring

TMAH degradation progress was monitored over time by measuring both dry weight loss and lignin absorbance in UV spectroscopy. The degradation efficiency of O_2 plasma reactor was monitored by following

the dry weight loss and FTIR spectra.

For TMAH degradation, dry weight loss was calculated at the end of the experiment by filtering the solution using a 0.2 μm nylon filter on a Büchner funnel, and the filter containing the residual organic matter was subsequently weighed. For O_2 plasma reactor degradation, dry weight loss at the end of the experiment was calculated by weighing the crucible containing the combustion residue.

UV-Visible absorption spectra were acquired using a Thermo-scientific Genesys 50 UV-Vis spectrophotometer.

Reference lignin (Cat. N∘ 471003: alkali lignin with low sulfonate content) was obtained from Sigma Aldrich and used for UV-Vis calibration of the lignin concentration in solution. A correlation coefficient of $r^2 = 0.99$ was obtained for this calibration.

Spectra were recorded for three replicates of bark mixed with TMAH solution and bark mixed with TMAH control solution diluted to 1/10 concentration. Spectra for each sample was acquired over the 200–600 nm wavelength range at 1 nm resolution and corrected from TMAH control solutions.

For FTIR analysis, a KBr pellet was prepared by mixing 2 mg of bark powder with 198 mg of KBr, followed by compression using a KBr pellet press machine. FTIR spectra were recorded using a Thermo Scientific Nicolet iN MX microscope equipped with an Ever-Glo conventional Infrared source, a x15 objective, and a liquid nitrogen-cooled mercury cadmium telluride (MCT)-A detector. Data analysis was performed using OMNIC Picta software.

2.7. Efficiency recovery experiments

AuNPs were obtained from NanoComposix (San Diego, CA, USA) as certified reference materials provided in aqueous suspension, with a nominal diameter of 32.7 ± 2.0 nm and a certified particle number concentration (0.147 × 10^9 NPs·mL^{-1}). Metal oxide NPs (Fe_2O_3, MnO_2, TiO_2, Al_2O_3, and CuO) were supplied in powder form by different manufacturers. According to supplier specifications, CuO NPs (US Research Nanomaterials) had a nominal size range of 30–50 nm, Fe_2O_3 NPs (US Research Nanomaterials) a nominal diameter of 100 nm, MnO_2 NPs (US Research Nanomaterials) a nominal diameter of 50 nm, Al_2O_3 NPs (Sigma-Aldrich) a nominal size < 50 nm, and TiO_2 NPs (Tayca Corporation) a nominal diameter of 100 nm. No surface coating or stabilizing agent was specified by the manufacturers, and no additional surface functionalization was applied prior to use. Fe_2O_3, MnO_2, TiO_2, Al_2O_3, and CuO NPs were futher characterized using scanning electron microscopy (SEM-EDS). The SEM pictures and size results are presented in Supporting Information 1.

To evaluate the NPs recovery after bark degradation using either TMAH or O_2 plasma methods, the 'pristine' bark sample from the Fontainebleau forest was doped with the selected engineered NPs above mentioned. Spiking experiments consisted of adding known masses of engineered nanoparticles to pristine bark samples prior to degradation, followed by digestion and spICP-MS analysis to assess nanoparticle recovery. An initial test of two replicates with gold NPs was carried out, prior the use of a mixture containing Al_2O_3, CuO, TiO_2, MnO_2 and Fe_2O_3 NPs in MQ water, with respectively 3 replicates and 10 replicates for TMAH and O_2 plasma degradation. Another NPs aliquot was added to MQ water as a reference and stored in the fridge until the analysis. The NP mixture solution was prepared to reflect environmentally relevant concentrations in urban bark samples, based on calculations from recent data reported by our group [27]; see Supporting Information 2). For TMAH degradation 1 mL of the NPs mixture was added to the bark in 20 %V/V TMAH solution while a 100 μL droplet of the NPs mixture was added to the bark before O_2 plasma degradation. All samples were systematically sonicated during 20 min prior to analysis to limit aggregation. The effect of the bark degradation on the NPs was assessed through the monitoring of the particle number concentration (PNC), particle mass concentration (PMC) and particle mass distribution (PMD) for undegraded spiked samples (only NPs), degraded spiked bark samples and for the unspiked degraded control bark sample. These parameters were quantified using single-particle inductively coupled plasma mass spectrometry (spICP-MS). The protocol is illustrated in the Fig. 1.

2.8. NPs detection by sp-ICP-MS

Single-particle ICP-MS measurements were performed using an analytical workflow previously developed and fully validated on the same HR-ICP-MS instrument (Element II, Thermo Scientific, located on the IPGP – PARI platform), including particle mass calibration, size detection limits, linearity range, accuracy, and repeatability, as detailed in Tharaud et al. [39,40]. All measurements were conducted within the validated operational range of this well-established method. The introduction system was a quartz cyclonic spray chamber with a PFA MicroFlow nebulizer. The peristaltic pump rate was set at 12 revolution per minutes (rpm) generating a sample uptake flow of 0.171 $mL.min^{-1}$. Torch parameters were optimized to achieve maximum sensitivity and stability: the RF power was set to 1285 W, the auxiliary flow rate at 1 $L.min^{-1}$, the cooling flow rate at 16 $L.min^{-1}$, and the sample flow rate at 1.025 $L.min^{-1}$. The HR-ICP-MS was tuned daily to ensure maximum sensitivity (ie 1.6–2E6 ct s^{-1}/ppb on ^{115}In in Low Resolution mode) and stability while also maintaining the oxide rate (UO/U) below 10 %. Secondly, high-resolution lenses were optimized in order to reach the best resolution power in each resolution mode (MR > 400; HR > 10000). The medium resolution was chosen to analyze ^{197}Au, ^{27}Al, ^{48}Ti, ^{55}Mn, ^{56}Fe and ^{63}Cu. For a 90 s time scan and with a dwell time of 3 ms, a total of 15 000 data points were acquired per sample. The number of events did not exceed 10 % of the total readings, i.e. 1500 particles. To determine the transport efficiency, a certified Au NPs reference material (i.e. diameter = 32.7 ± 2.0 nm and particle concentration 0.147 ×10^9 NPs. mL^{-1}) was used [39]. A transport efficiency of 11.1 % was calculated. The quantification was carried out using a multi-elemental standards range with concentrations varying from 100 ppt to 10 ppb.

For a given type of NP, identical dilution factors (from 100 to 1000) were applied before analysis to the digested, undigested and control samples. For each sample, a time-resolved signal intensity trace is acquired, displaying counts per second as a function of analysis time. Discrete signal peaks correspond to individual nanoparticle events, whereas the continuous baseline signal reflects the contribution from the dissolved ionic fraction. Particles larger than approximately 1–2 μm are known to be excluded by the sample introduction system and were therefore outside the analytical scope of the present study.

To distinguish the dissolved fraction from the particulate fraction, the Gaussian Mixture Model (GMM) has been used [40]. The GMM is based on a model that gives probabilities for all the datapoints to belong to a specific cluster, here the dissolved fraction or the particulate fraction. Once the data points have been distributed to the clusters, the number and mass of particles can be recalculated [39].

Then the particle mass concentration for one dataset is recalculated using the equation (1):

$$\mathrm{PMC}\frac{\sum mp}{q * td * \quad \eta transport} \tag{1}$$

where *mp* is the mass of the particles, *td* the sample analysis duration, *q* the sample uptake flow and η*transport* the transport efficiency. Recoveries were calculated by comparing spiked reference solutions (ie without bark and undigested) and spiked bark samples after digestion, after correcting the latter by subtracting the PNC and PMC measured in control (non-spiked) bark samples.

Particle mass recovery and particle number recovery were calculated using the Eq. (2) and (3):

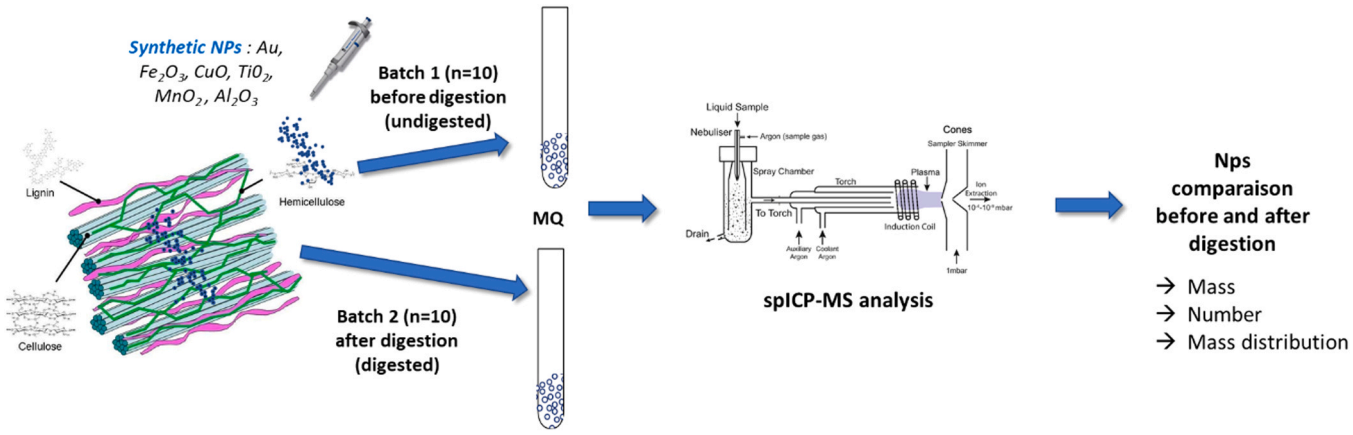

Fig. 1. Recovery test protocol.

$$\text{NPs mass recovery} = \frac{\left(\sum_{1}^{n} PMC\ (after\ digestion)\right) / n)}{\left(\sum_{1}^{n} PMC\ (before\ digestion)\right)/n)} \quad (2)$$

$$\text{NPs number recovery} = \frac{\left(\sum_{1}^{n} PNC\ (after\ digestion)\right) / n)}{\left(\sum_{1}^{n} PNC\ (before\ digestion)\right)/n)} \quad (3)$$

where n is the number of replicates and PNC the particle number concentration. The mass of the element and not the mass of the oxide was used for the calculation. The PMC and PNC values of the control bark were subtracted from each digested spiked sample. Because particle size determination is derived from particle mass under the assumption of spherical geometry, which may not be valid for all investigated NPs, mass-based particle distributions were preferentially used to assess nanoparticle transformations during selective degradation process.

Complete digestion of samples was performed as a complementary control, and quadrupole ICP-MS was used solely for the routine determination of total elemental concentrations following established laboratory protocols (see Supporting Information 3).

3. Results and discussion

3.1. Localization of inorganic particles in bark samples

To investigate the distribution and nature of inorganic particles within bark samples, a multi-scale imaging approach was employed, beginning with bulk surface observations and progressing to fine-resolution, 3D, and elemental analyses. Initial bulk surface observations were conducted using scanning electron microscopy (SEM) in backscattered electron (BSE) mode on bark samples collected from urban environments. In the resulting images (Fig. 2 A), the organic matrix appears dark, while bright regions indicate metallic particles. These particles, exhibiting heterogeneous size distributions from nanometers to microns, are often localized in the bark's porous and recessed structures suggesting the bark morphology facilitates atmospheric particle entrapment (Fig. 2 C). While some particles reside on the surface, others are embedded within the organic matrix. Energy-dispersive X-ray spectroscopy (EDX) confirmed the presence of metallic compounds, notably iron and copper oxides, as well as trace elements including chromium, zinc, barium, and tin (Fig. 2B).

While SEM-EDX confirmed particle presence on the bark surface, it lacked the ability to assess particle distribution through the sample volume. To address this, X-ray microtomography (micro-CT) was employed. High-density regions, attributed to metal-containing particles, were identified via bright voxels in the micro-CT images. The 3D reconstruction (Fig. 3A) revealed a scattered distribution of such particles within the bark volume (from surface to core). Virtual 2D

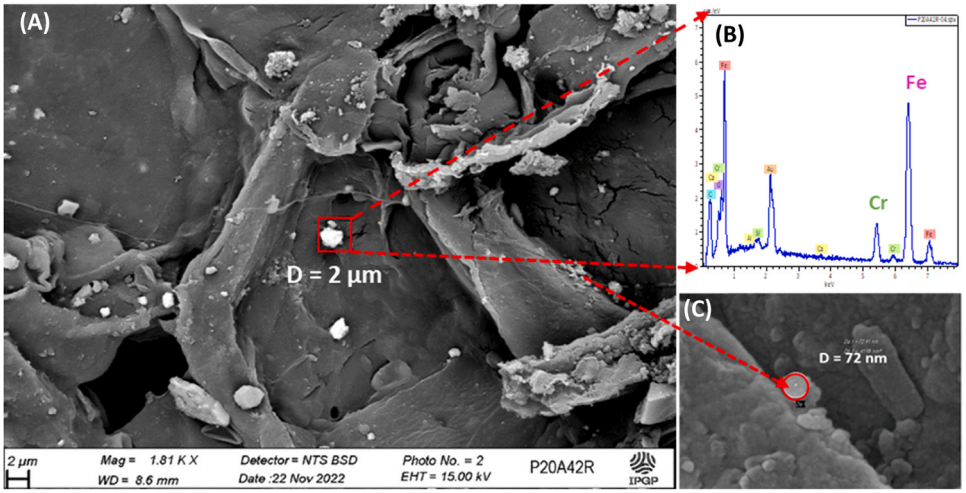

Fig. 2. SEM image of P20A42 sample. Metallic particles on the bark surface (A). EDS spectrum associated with one particle, C) Image of a nanoparticle.

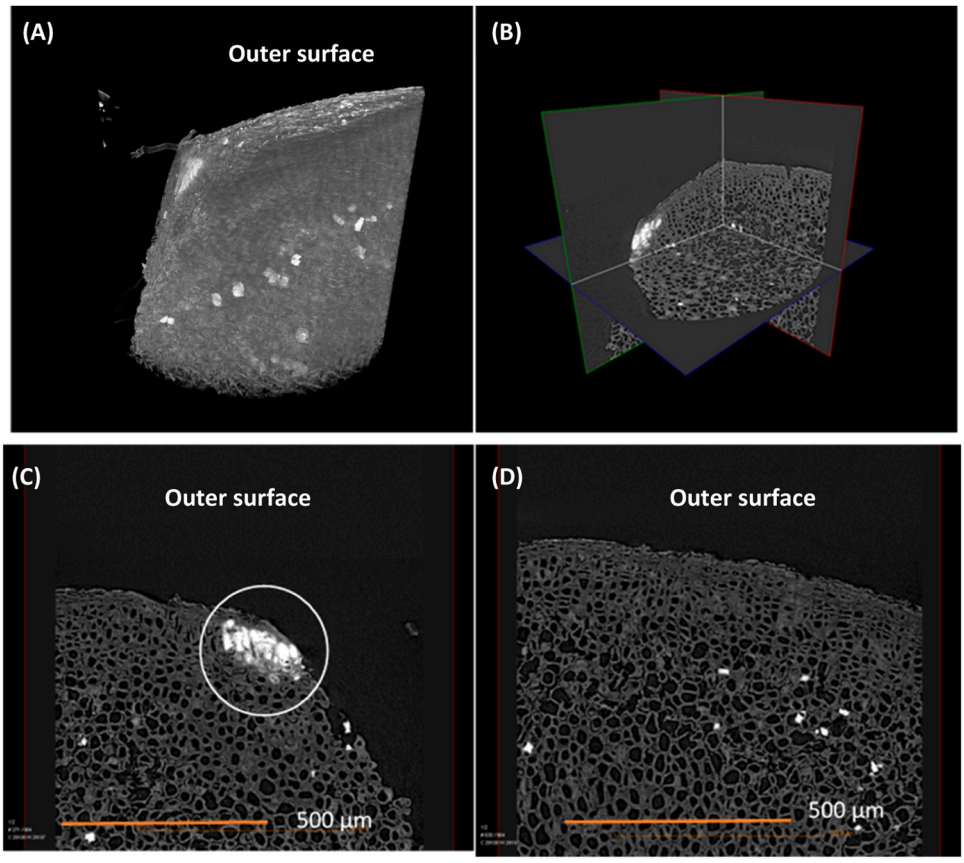

Fig. 3. 3D imaging of sample P20A44R obtained by micro-CT (1vx=1 µm). 3D reconstruction (A). 2D virtual slices extracted from (A) with various orientation (B, C, D).

orthoslices (Fig. 3C-D), extracted from the reconstructed volume, enabled detailed examination of micrometric particles localization. One slice (Fig. 3 C) highlighted a large region accumulating dense particles (~200 × 50 µm) near the bark–air interface, supporting the hypothesis that bark serves as a primary filter for airborne particles. X-ray fluorescence mapping (micro-XRF) further confirmed the presence of iron in this region, suggesting an anthropogenic origin. Another orthoslice (Fig. 3D), showed more uniform particle distributions, indicating potential penetration into deeper layers.

To further explore particle penetration, 500 nm-thick bark cross-sections were prepared and analyzed using SEM-EDX. The outer region consists of compact cells, while the inner bark contains loosely packed, larger cells (Fig. 4A). Numerous cavities were observed, possibly resulting from resin artifacts or natural voids. Elemental mapping (Fig. 4B) demonstrated that iron-rich particles were primarily concentrated in the outermost and innermost regions, with minimal presence in the intermediate zone. This distribution suggests selective retention at structural interfaces. Finally, transmission electron microscopy (TEM) provided nanoscale insights into particle morphology (Fig. 4C). EDX analyses confirmed the presence of iron oxide NPs forming aggregates between 50 and 500 nm, with individual NPs as small as 10 nm. Morphologies ranged from spherical to rod-like forms. Additional elements, including silicon and aluminum, were also detected, though their distribution patterns differed from that of iron. Selected area electron diffraction (SAED) analysis (Fig. 4D) was used to identify the crystalline nature of one of the iron-containing particles embedded in the bark cross-section. The SAED results revealed that the red and green vertical lines correspond to the expected diffraction peak positions of two iron oxide phases: magnetite (Fe_3O_4) and hematite (Fe_2O_3), respectively.

Previous studies have investigated heavy metal retention in tree bark using non-destructive PIXE (Particle-Induced X-ray Emission) and ICP-MS techniques [30,41]. These works showed that atmospheric contaminants accumulate predominantly in the outer bark (suber). One study further demonstrated that although most particles are retained near the surface, limited diffusion into cortical tissues may occur, likely due to oxide dissolution and subsequent metal ion migration. This finding aligns with our fine-section maps and micro-CT results, although such diffusion mechanisms were not directly explored in the present study. Therefore, in order to obtain a quantitative,rather than merely qualitative, measurement of the NPs trapped within the bark, the organic matrix must be completely degraded. This requires a selective degradation protocol that ensures full removal of the bark material without altering the physicochemical properties of the inorganic NPs.

3.2. Bark degradation monitoring

While TMAH degradation led to a corrected dry weight loss of 27 %, the highest loss was achieved with O_2 plasma treatment, reaching 89 % of dry weight loss.

Figure A displays, according to the wavelength and for different time steps, the absorbance of the three TMAH digestates corrected from the bark absorbance alone. Peak intensity at the wavelength of 220 nm is observed at each time step. This peak is characteristic of the lignin molecule [42]. During the degradation, the intensity of this peak increases proportionally to the extent of bark decomposition. In the presence of TMAH, Δ-Absorbance at 220 nm changes from 0.48 ± 0.05–2.56 ± 0.16 A.U. It raises after few hours and plateaus at 30 h. A peak corresponding to the release of phenolic compounds from lignin appears in the region 270 and 280 nm after 23 h [43,44]. The Δ-Absorbance associated to this wavelength increases from 0.24 ± 0.038–2.19 ± 0.25 A.U. The total lignin concentration in the TMAH

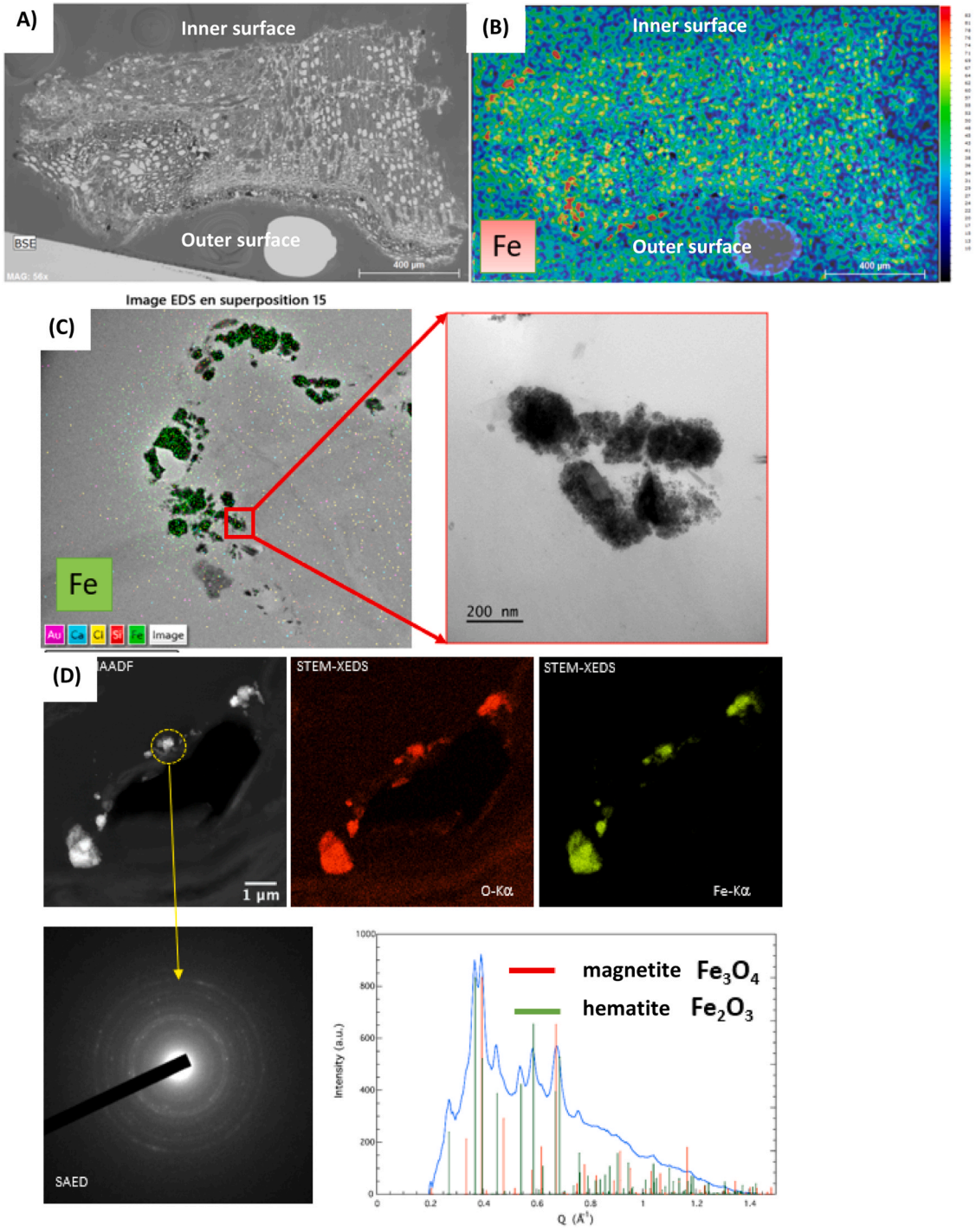

Fig. 4. Images of ultrathin bark sections (500 nm thick) from sample P20A41R. SEM image in backscattered electron mode (A). SEM elemental mapping of iron (B). TEM-EDS images (C). SAED analysis (D).

digestion solution (Fig. 5B) reached 1.9 mg.mL^{-1}. Assuming a total lignin content of 50 wt% in the bark [29], this corresponds, in the present case, to a maximum potential release of 2 mg·mL^{-1} total lignin into TMAH from the bark. This indicates that TMAH induced the dissolution of approximately 97 % of the total lignin.

Fig. 6A displays for the raw bark sample all the characteristic peaks of lignin [45,46]. These peaks disappeared in the IR spectra of the digested bark sample (Fig. 6B). Namely, the aromatic C-H in-plane deformation at 1091 cm^{-1}, C-O and glucopyranosic cycle syringyl symmetric vibration at 1230 cm^{-1}, stretching vibrations in the aromatic ring at 1426 cm^{-1} and 1508 cm^{-1}, and C═O stretching at 1620 cm^{-1}. Similarly, most of the peaks corresponding to cellulose and hemicellulose also disappear after O_2-plasma degradation, including C-O-C stretching at 1091 cm^{-1}, CH bond deformation at 1458 cm^{-1}, and the stretching vibration of the C═O functional groups of the acetyl ester at 1508 cm^{-1} whereas some others remain, namely CH2 wagging at 1319 cm^{-1} and C-H deformation at 1385 cm^{-1}. Although,very simple C chains were not affected by degradation and remain (-CH, -CH_2 bonds, and C═C),these results highlight the efficiency of O_2 plasma for bark degradation.

On the basis of dry weight loss results, lignocellulosic solubilisation and/or degradation, the O_2 plasma reactor appears to be the most

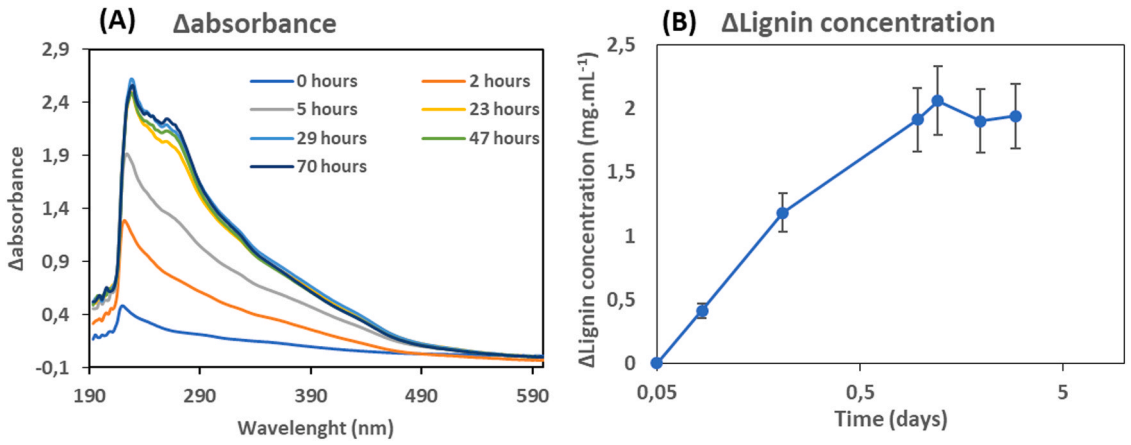

Fig. 5. The absorbance of the bark was subtracted from that of bark + TMAH. This Δabsorbance is plotted as a function of the wavelength in (A). The lignin concentration of the bark is subtracted from that of the bark + TMAH this Δlignin concentration is plotted as a function of time in (B).

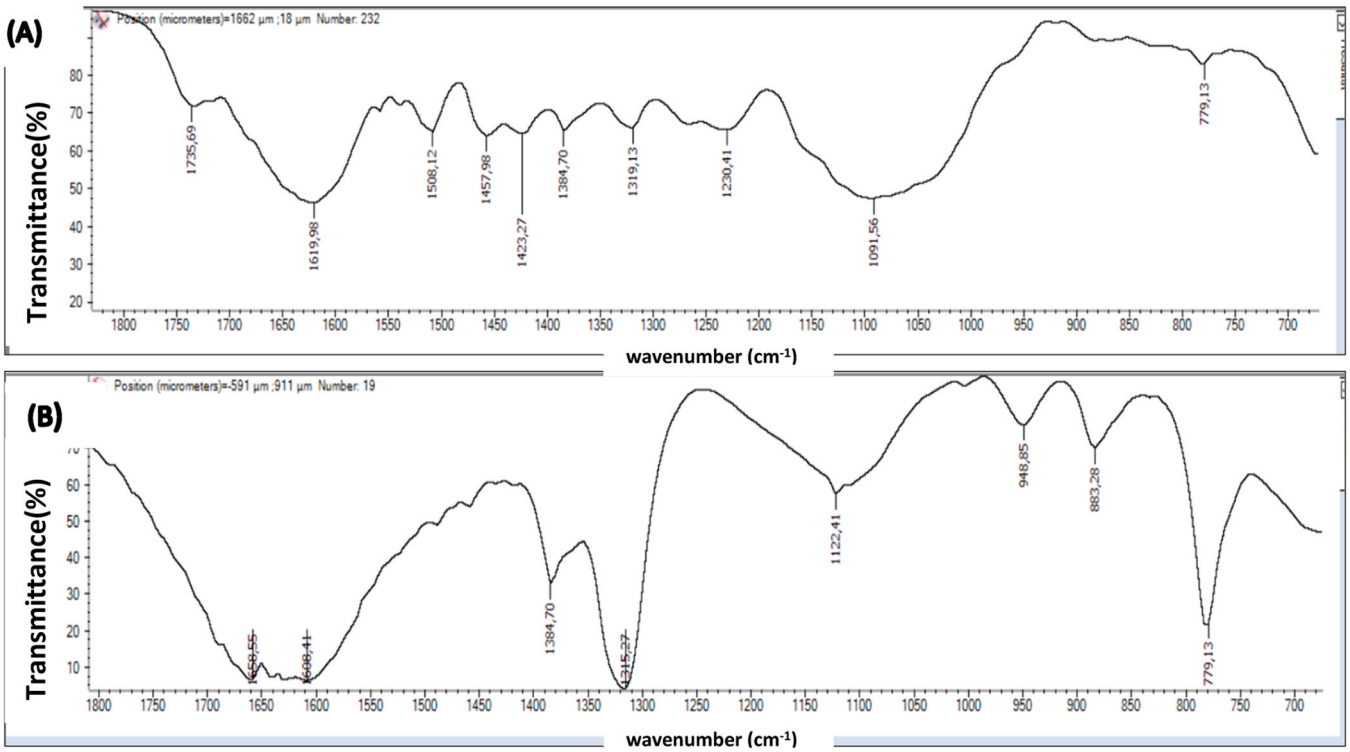

Fig. 6. FTIR spectra of bark before (A) and after O_2 plasma degradation (B).

efficient "soft" methods to degrade tree bark powder. Hence, it remains necessary to accurately evaluate the potential effect of O_2 plasma and TMAH degradation on the inorganic NPs themselves.

3.3. Nanoparticle stability during degradation

The effect of TMAH and O_2 plasma bark degradation on metallirganic NPs was assessed by calculating the NPs number recovery, NPs mass recovery and mass distributions before and after the bark degradation, for each type of NPs.

3.3.1. O_2 plasma degradation recovery experiment

PMC and PNC of Fe_2O_3, NPs, Al_2O_3 NPs and TiO_2 NPs are displayed in Table 1. NPs of Fe_2O_3, Al_2O_3, and TiO_2 were detected, while no CuO or MnO_2 NPs initially introduced into the system were observed after degradation. Instead, dissolved Cu and Mn ions were detected, indicating their release into the solution.

Table 1
Particle mass and number concentrations before and after O_2 plasma degradation.

Nanoparticle	PMC Before (ng·mL^{-1})	PMC After (ng·mL^{-1})	PNC Before ($\times 10^9$ NPs·mL^{-1})	PNC After ($\times 10^9$ NPs·mL^{-1})
Fe_2O_3 (n = 10)	101.3 ± 20.2	57.6 ± 27.0	6.4 ± 1.1	8.9 ± 4.5
Au (n = 3)	0.015 ± 0.002	0.015 ± 0.003	0.0012 ± 0.0001	0.0017 ± 0.0001
TiO_2 (n = 10)	16.2 ± 4.5	14.8 ± 2.4	7.1 ± 1.8	7.8 ± 2.4
Al_2O_3 (n = 10)	86.5 ± 17.9	87.5 ± 17.2	27.0 ± 6.7	27.0 ± 8.0

The effects of degradation on nanoparticle concentrations were

assessed by comparing the mean particle mass concentration (PMC) and particle number concentration (PNC) before and after the degradation process (Table 1). For Fe_2O_3 NPs, a substantial reduction in PMC was observed dropping by 43 % (Table 1) suggesting partial dissolution. Despite this decrease in mass, the PNC remained relatively stable. In contrast, the PMCs of Au, TiO_2, and Al_2O_3 NPs remained effectively unchanged (Table 1), indicating greater mass stability under the same conditions. The PNCs of TiO_2 and Al_2O_3 also showed minimal variation.

For Au NPs, the mean mass recovery was 101 ± 13 %, while the mean particle number recovery reached 138 ± 12 %, suggesting potential particle fragmentation during the treatment, while the constant PMC indicates that the total mass of Au remained unchanged. In the case of Fe_2O_3, TiO_2, and Al_2O_3 NPs, the mean mass recovery rates were 57 ± 44 %, 92 ± 34 %, and 101 ± 28 %, respectively. Corresponding mean particle number recovery rates were 139 ± 71 % for Fe_2O_3, 110 ± 41 % for TiO_2, and 100 ± 39 % for Al_2O_3. These results suggest higher variability in mass-based recovery for Fe_2O_3, along with a general tendency for number-based recoveries to exceed 100 %, potentially due to particle fragmentation effects, or analytical sensitivity limits. Both CuO and MnO_2 NPs seemed to be completely degraded by the O_2 plasma treatment. To check how much metal remained, a mass balance was done by comparing the total metal concentration (NPs plus dissolved metal) before treatment and the dissolved metal left after treatment.

For copper, the total concentration dropped from 125 ± 38 ng·mL^{-1} to 88 ± 23 ng·mL^{-1} . For manganese, it dropped from 0.055 ± 0.007 ng·mL^{-1} to 0.023 ± 0.005 ng·mL^{-1} . This means about 30 % of the copper and 58 % of the manganese were lost overall. These losses show that the remaining dissolved metal cannot fully account for the NPs that disappeared, suggesting that, besides partial dissolution, another process such as volatilization may also be involved during the oxygen plasma treatment.

Despite the relatively high RSD values observed for certain nanoparticle types, these results are based on a statistically meaningful number of independent experiments (n = 10 for O_2 plasma and n = 3 for TMAH) and reflect the intrinsic variability of nanoparticle–matrix interactions rather than a lack of experimental reproducibility.

Effect of O_2 plasma on NPs stability: for the Au, Fe_2O_3, TiO_2 and Al_2O_3 NPs the particle mass distribution (PMD) before and after degradation is represented using histograms (Fig. 7). The frequency of data in each bin is divided by the maximum frequency of all the data, in order to abstract from the total number of particles, highlighting only the relative distribution of masses. This ensures a direct comparison of distribution profiles, regardless of differences in overall data quantity before and after degradation. The PMD results are reproducible, with an uncertainty below 5 %, indicating reliable measurements across replicates.

The shape of the Au and TiO_2 NP histograms remains nearly identical before and after degradation, indicating high stability of the PMD (Fig. 7). For Al_2O_3 NPs, a narrowing of the distribution is observed after degradation. In contrast, Fe_2O_3 NPs exhibit a marked shift in the distribution towards lower masses.

Hence, the near 100 % mass and number recovery rates of Au, TiO_2 or Al_2O_3 NPs further suggest that O_2 plasma degradation does not significantly affect these NPs. In contrast, Fe_2O_3 NPs exhibit a mean loss of 43 % in mass fraction, despite a stable particle number concentration (PNC). This loss of Fe_2O_3 material could result from either aggregation or partial dissolution. However, since aggregation would likely reduce the PNC, and the PNC remains stable (albeit with high variability after degradation), partial dissolution is the more plausible explanation.

Total mass recovery (protocol in Supporting Information 3), as analyzed by ICP-Q-MS, yielded the following results: 62 ± 25 % for Fe_2O_3, 104 ± 31 % for TiO_2, 95 ± 37 % for Al_2O_3, 76 ± 16 % for CuO, and 50 ± 10 % for MnO_2 NPs. These findings correspond to mean nanoparticle losses during the degradation process of 38 %, 24 %, and 50 % for Fe_2O_3, CuO, and MnO_2 NPs, respectively.

The O_2 RF plasma system uses an RF-induced gaseous discharge to degrade organic material primarily through oxidation. This process requires an ionization energy of 13.6 eV. Oxygen plasma, composed mainly of O^+ ions, promotes the oxidation of organic matter and can also affect certain metal oxides. The oxidation of organic material generates organic fragments, volatile products (e.g., CO_2 and H_2O), phenolic (RCOH*) and oxygenated (OH•) radicals. Water formed during this process can further react with O^+ ions to produce additional OH• radicals, which may capture free electrons present in the plasma, leading to the formation of hydroxide (HO^-) ions [47]. When metallic oxide NPs interact with plasma radicals and ions, they may undergo oxidation. Among the tested oxides, MnO_2 is the only NP for which the metal (Mn) is capable of significant oxidation, transitioning from an oxidation state of + 4 to + 7, forming permanganate ions (MnO_4^-). In contrast, the metals involved into CuO, Fe_2O_3, TiO_2, and Al_2O_3 NPs are less prone to oxidation. Ti and Al are already in their highest oxidation state (Ti^{4+} in TiO_2 and Al^{3+} in Al_2O_3) and while higher oxidation states exist for CuO and Fe_2O_3, further oxidation would lead to unstable compounds that readily revert to their original oxide forms [48].

The ionization energies for these oxides, corresponding to the energy required to ionize their primary element, are as follows: 3.6 eV for CuO, 12.7 eV for Fe_2O_3, 13.7 eV for TiO_2, and 16.0 eV for Al_2O_3 [49]. These values indicate that CuO and Fe_2O_3 may undergo partial ionization, forming Cu^{2+} and Fe^{3+} ions in the plasma. However, the higher ionization energies of TiO_2 and Al_2O_3 prevent significant ionization, allowing these NPs to remain in their neutral nanoparticulate form.

For Fe_2O_3, the similarity in ionization energies between Fe–O^{3-} and O–O bonds suggests that ionization may occur only at the nanoparticle surface, leaving the core intact. A fraction of the ions generated in the plasma is likely evacuated by the reactor pump, contributing to the observed losses of Fe_2O_3, CuO, and MnO_2 NPs during degradation. This is consistent with the decreased total Cu and Mn content measured by spICP-MS after plasma treatment. Approximately 43 ± 11 % of the total Fe_2O_3 mass undergoes surface ionization, and 38 ± 25 % of the ionized fraction is evacuated by the reactor pump, explaining the 57 ± 44 % mass recovery rate observed after O_2 plasma degradation. The histograms of Fe_2O_3 NPs show a shift toward lower masses, reflecting size reduction due to surface ionization and material loss (Fig. 7). Once the O_2 plasma is off, any remaining MnO_4^- and Cu^{2+} ions in the plasma revert to their stable forms. MnO_4^- could bind with counter ions such as K^+, forming $KMnO_4$, while Cu^{2+} would combine with OH^- ions formed during organic matter oxidation to form $Cu(OH)_2$. Upon resuspension in MQ water (pH = 6), $KMnO_4$ dissociates completely, releasing MnO_4^-, a highly water-soluble species. Similarly, $Cu(OH)_2$ dissociates under these conditions ($pK_s = 19.7$), releasing some Cu^{2+} ions into the solution.

The resulting MnO_4^- and Cu^{2+} ions account for the increased dissolved fractions observed after degradation and explain the complete dissolution of MnO_2 and CuO NPs.

3.3.2. TMAH degradation recovery experiment

PNC et PMC before and after degradation for each type of engineered NPs are displayed in the Table 2.

A mean mass number recovery of 66 ± 17 % and a mean mass recovery of 43 ± 17 % were obtained during the AuNPs spiking experiments. For the other targeted NPs, both the particle mass concentration (PMC) and particle number concentration (PNC) were higher after degradation. Recovery rates for these NPs exceeded 100 %, with PNC overestimated by factors ranging from 1.2 to 13.2 and PMC overestimated by factors of 2.5–10.6.

Despite these discrepancies, the total metal mass balances, measured after leaching from the tube walls using ICP-MS QUAD, confirmed mass balances of 94 ± 8 % for Fe_2O_3, 86 ± 13 % for TiO_2, 99 ± 4 % for Al_2O_3, 110 ± 49 % for CuO, and 96 % for MnO_2 NPs. These findings validate the accuracy of the results obtained in TMAH experiments.

These unexpected recovery values of NPs in TMAH solutions can be explained by the following facts. A significant adsorption of NPs on the tube walls in MilliQ water at pH values ranging from 5 to 6. Under such

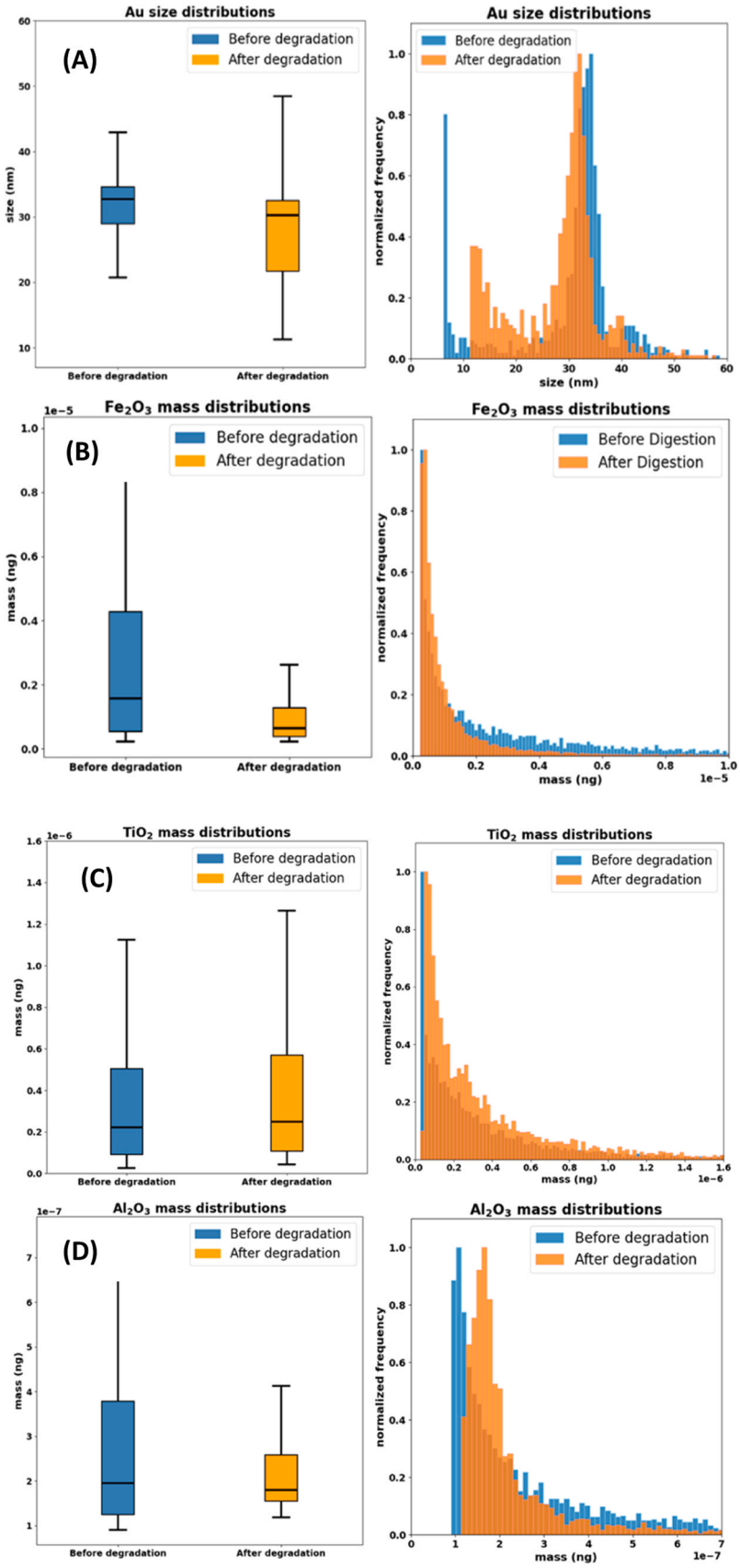

Fig. 7. Boxplot and histograms of the concatenate PMD results before and after O_2 plasma degradation for AuNPs (A). Fe_2O_3 NPs (B). TiO_2 NPs (C) and Al_2O_3 NPs (D).

Table 2
Particle Mass and Number Concentrations Before and After TMAH Degradation.

Nanoparticle	PMC Before ($ng \cdot mL^{-1}$)	PMC After ($ng \cdot mL^{-1}$)	PNC Before ($\times 10^9$ $NPs \cdot mL^{-1}$)	PNC After ($\times 10^9$ $NPs \cdot mL^{-1}$)
Fe_2O_3 (n = 3)	37.0 ± 4.6	91.1 ± 63.5	0.053 ± 0.014	0.42 ± 0.05
Au (n = 3)	0.0013 ± 0.001	0.00084 ± 0.00014	0.00028 ± 0.00001	0.00012 ± 0.00005
TiO_2 (n = 3)	0.018 ± 0.003	0.1 ± 0.03	0.38 ± 0.28	5.0 ± 0.8
Al_2O_3 (n = 3)	0.2 ± 0.1	1.4 ± 0.1	3.2 ± 1.2	19 ± 2
CuO (n = 3)	0.021 ± 0.001	0.083 ± 0.019	0.049 ± 0.037	0.061 ± 0.011
MnO_2 (n = 3)	0.3 ± 0.0	1.5 ± 0.1	3.0 ± 0.4	12 ± 1

conditions, increased adsorption onto the tube walls leads to underestimation of reference values, introducing bias in the calculated recovery rates (these effects are discussed in detail in appendices). Conversely in the TMAH conditions, the presence of organic molecules and the high pH value (i.e. pH=11) promote the stability of NPs suspension. At this pH, organic matter facilitates the desorption of metal oxide NPs from tube surfaces by enhancing negative electrostatic interactions between the particles and the tube walls. Additionally, organometallic complexes may form, further preventing particle adhesion [50].

Therefore, MilliQ water is not a suitable reference media for assessing NP recovery rates (in terms of PNC or PMC) during degradation with TMAH [51,52]. Instead, comparing the particle mass distribution (PMD) before and after degradation provides a more accurate assessment of the effects of TMAH treatment on nanoparticles.

The mass distribution data for each type of NP before and after degradation are displayed using histograms and boxplots in Figs. 8A and 8B. The PMD results were reproducible, with an uncertainty below 5 %, indicating reliable measurements across replicates, then concatenated. TiO_2 and MnO_2 NPs show similar mass distributions before and after degradation, although a slight shift towards higher masses is observed. Overall, TiO_2, Al_2O_3, and MnO_2 NPs exhibit stable particle mass distributions (PMD) following TMAH treatment, indicating that this degradation method does not alter their properties. In contrast, Fe_2O_3 and Au NPs show a significant shift towards lower masses. For CuO NPs, a marked shift towards higher masses is observed in the histograms (Fig. 8A).

Behavior of Fe_2O_3 NPs During TMAH Degradation**:** The shift toward lighter particles observed for Fe_2O_3 NPs after TMAH degradation suggests that the degradation process causes either the partial dissolution or the disaggregation of the original NPs. At pH 11, Fe_2O_3 NPs carry a negative charge, which typically prevents aggregation or disintegration due to electrostatic repulsion [53]. This negative charge stabilizes the particles, keeping them dispersed in suspension. Hematite is generally a stable and sparingly soluble phase, even under basic conditions [53]. A simulation of hematite nanoparticle behavior at pH 11 was performed using Visual Minteq version 3.1. The results show that NPs initially added remain in the solid precipitate form. However, when fulvic acid—used as an analogue for the organic ligand of TMAH—is included in the simulation at a concentration of 8 g/L, the solid hematite completely dissolves, and iron forms a soluble organometallic complex. Nevertheless, Fe_2O_3 NPs are detected in the TMAH solution. This indicates that hematite NPs undergo only partial dissolution. This partial dissolution would be enhanced by organic matter, particularly at the surface or defects in the crystalline structure [50]. Thus, the surface dissolution of Fe_2O_3 NPs is promoted by both the basic medium and the organic matter, resulting in a selective process that gradually reduces the nanoparticle size.

Behavior of CuO NPs During TMAH Degradation: The increase in NP mass suggests that the smallest CuO particles may dissolve during degradation and/or the remaining particles form aggregates. At pH 11, near the point of zero charge (PZC) of CuO (approximately 10) [54], the electrostatic repulsion between CuO particles decreases significantly and creates favourable conditions for homoaggregation, where smaller CuO particles cluster into larger aggregates [55]. In addition, during the TMAH degradation, organic matter and specifically carboxylate groups ($-COO^-$) and other functional moieties from bark degradation, interacts with CuO NPs. It can adsorb onto the CuO surface and modify their surface chemistry [56–58]. This process can both reduce a potential dissolution, and simultaneously facilitate aggregation by reducing surface charge repulsion [59].

4. Conclusion

This study provides a detailed, multi-scale assessment of the localization and stability of inorganic NPs in tree bark. It also critically evaluates two degradation protocols, i.e. O_2 plasma and TMAH, for effectively removing the organic matrix while preserving NP integrity. Using advanced imaging and chemical analysis techniques, we demonstrated that atmospheric inorganic NPs, primarily iron and copper oxides, are distributed heterogeneously within the bark, accumulating preferentially at the outer surface and penetrating selectively into internal porous structures. Thus, the bark morphology acts as an efficient passive filter for urban airborne particles, with elemental mapping revealing anthropogenic signatures and selective retention at structural interfaces.

Our comparative analysis of the two degradation methods revealed that O_2 plasma treatment is markedly more efficient than TMAH digestion at removing organic matter (with up to 89 % dry weight loss observed). Spectroscopic monitoring confirmed the near-complete degradation of lignin and cellulose, thus validating O_2 plasma as an effective protocol for removing the organic matrix. However, the impact of these treatments on nanoparticle stability was found to be element-specific. O_2 plasma preserved the integrity of TiO_2 and Al_2O_3 NPs but induced the partial or complete dissolution of Fe_2O_3, CuO and MnO_2 NPs. This is due to differences in ionization energies and oxidation state transitions under plasma conditions. Conversely, TMAH degradation resulted in the partial dissolution of Fe_2O_3 NPs and the aggregation of CuO NPs, driven by the formation of complexes with organic ligands and changes in electrostatic interactions at high pH.

These findings highlight the need for a more refined degradation protocol that balances the efficient removal of organic matter with the preservation of all nanoparticle types. The observed variability in NP stability highlights the importance of tailoring methodological approaches to the specific physicochemical properties of targeted NPs. Moreover, our results emphasize that reference conditions (e.g., MilliQ water) may introduce significant bias in recovery assessments due to adsorption phenomena, further supporting the need for method optimization.

Importantly, this study provides a novel contribution by being, to our knowledge, the first to evaluate O_2 plasma and TMAH digestion specifically for the selective removal of lignocellulosic matrix in tree bark while systematically assessing their impact on the recovery and stability of embedded inorganic nanoparticles. This comparative evaluation establishes a methodological framework that can guide future studies on nanoparticle extraction from complex biological matrices.

Environmental implications

This study provides a robust methodology for detecting and quantifying atmospheric nanoparticles in tree bark, a passive bioindicator of urban contamination. By evaluating how different organic-matter degradation protocols affect nanoparticle stability and recovery under environmentally realistic concentrations, our work enables accurate assessment of the persistence, transformation, and potential hazard of metal and metal oxide nanoparticles in urban environments. These findings directly inform environmental monitoring strategies, improve risk assessment frameworks for emerging particulate contaminants, and

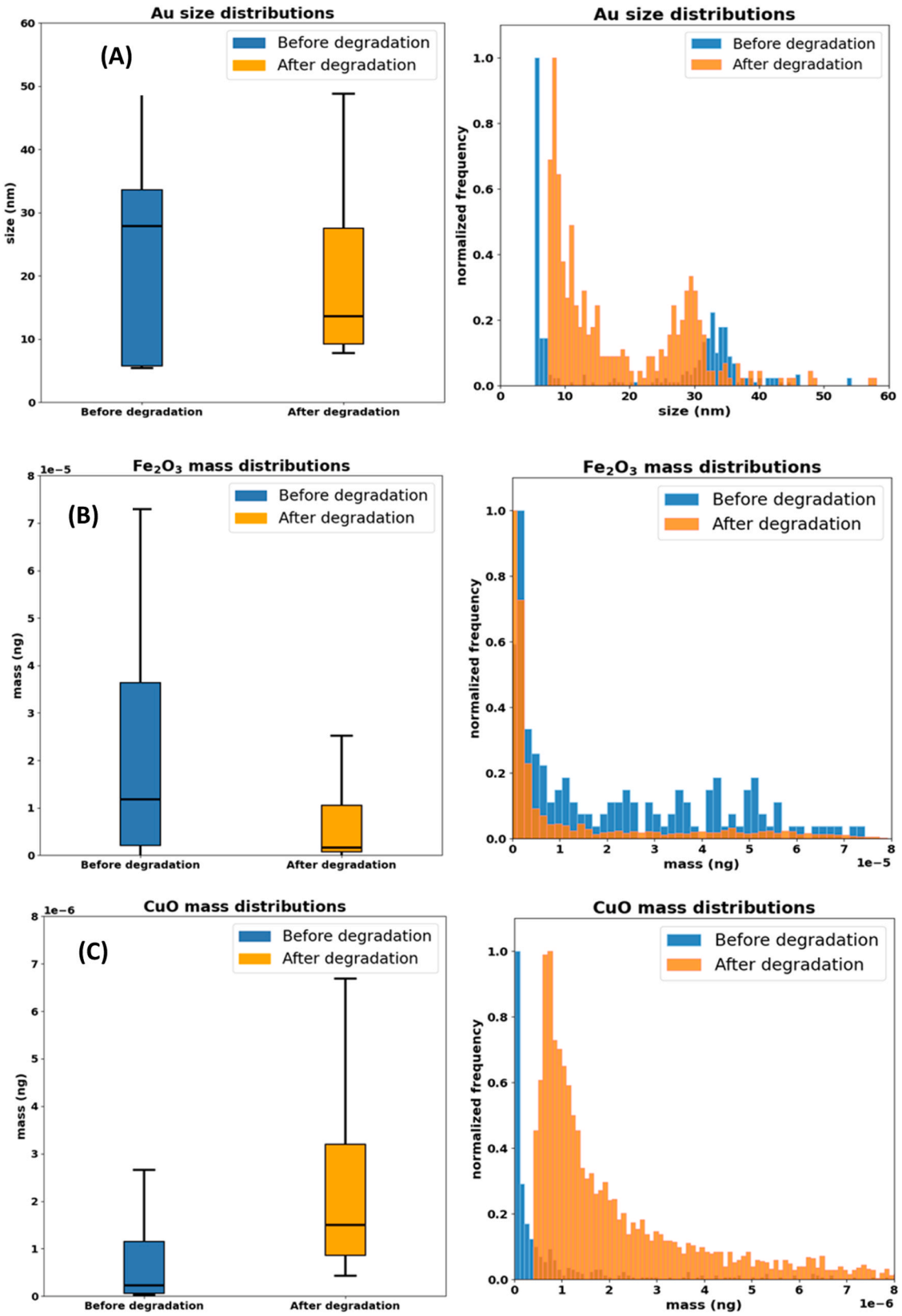

Fig. 8. A: Boxplot and histograms of the concatenate PMD results before and after O_2 plasma digestion for Au NP (A). Fe_2O_3 NPs (B) and CuO NPs (C). B: Boxplot and histograms of the concatenate PMD results before and after O_2 plasma digestion for TiO_2 NPs (D). MnO_2 NPs (E) and Al_2O_3NPs (F).

support the development of reliable analytical protocols for assessing nanoparticle fate in biologically and environmentally relevant matrices.

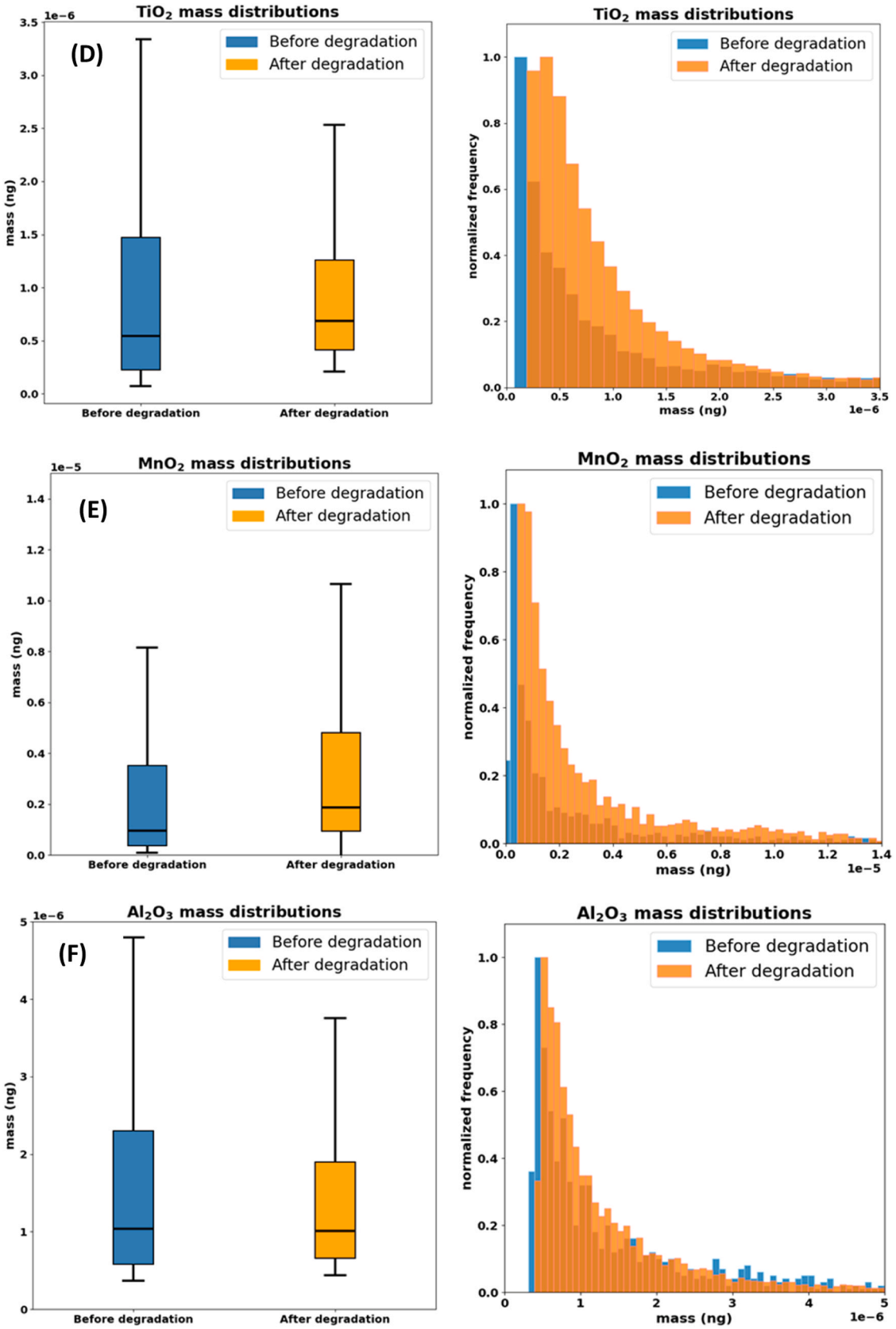

Fig. 8. (*continued*).

CRediT authorship contribution statement

Bérénice Piquet: Writing – review & editing, Validation, Formal analysis. **Mickaël Tharaud:** Writing – review & editing, Methodology, Investigation, Data curation. **Sophie Coural:** Writing – original draft, Methodology, Investigation, Formal analysis. **Yann Sivry:** Writing –

review & editing, Validation, Supervision, Project administration, Methodology, Investigation, Funding acquisition, Formal analysis, Conceptualization. **Marc F. Benedetti:** Writing – review & editing, Validation, Supervision, Methodology, Investigation. **Perrine Chaurand:** Writing – review & editing, Validation, Formal analysis.

Declaration of Competing Interest

The authors declare the following financial interests/personal relationships which may be considered as potential competing interests: Prof Yann SIVRY reports financial support was provided by Fondation Université Paris Cité. If there are other authors, they declare that they have no known competing financial interests or personal relationships that could have appeared to influence the work reported in this paper.

Acknowledgements

The authors would like to thank the Université Paris Cité IDEX funding of the NanoTrack Project in the frame of the "Dynamique Recherche" call 2019. We would also like to thank Fondation Université Paris Cité for supporting the NanObs (Observatoire Urbain Participatif des Nanoparticules). Some of this work was supported by the IPGP multidisciplinary program PARI, and by Paris–IdF region SESAME Grant no. 12015908. Three anonymous reviewers and the associate editor are thanked for their critical comments.

Appendix A. Supporting information

Supplementary data associated with this article can be found in the online version at doi:10.1016/j.jhazmat.2026.141584.

Data Availability

Data will be made available on request.

References

[1] Hochella, M.F., Mogk, D.W., Ranville, J., Allen, I.C., Luther, G.W., Marr, L.C., McGrail, B.P., Murayama, M., Qafoku, N.P., Rosso, K.M., Sahai, N., Schroeder, P.A., Vikesland, P., Westerhoff, P., Yang, Y., 2019. Natural, incidental, and engineered nanomaterials and their impacts on the Earth system. Science 363, eaau8299. https://doi.org/10.1126/science.aau8299.

[2] Mathissen, M., Scheer, V., Vogt, R., Benter, T., 2011. Investigation on the potential generation of ultrafine particles from the tire–road interface. Atmos Environ 45, 6172–6179. https://doi.org/10.1016/j.atmosenv.2011.08.032.

[3] Wagner, S., Funk, C.W., Müller, K., Raithel, D.J., 2024. The chemical composition and sources of road dust, and of tire and road wear particles–A review. Sci Total Environ 926, 171694. https://doi.org/10.1016/j.scitotenv.2024.171694.

[4] Trojanowski, R., Fthenakis, V., 2019. Nanoparticle emissions from residential wood combustion: a critical literature review, characterization, and recommendations. Renew Sustain Energy Rev 103, 515–528. https://doi.org/10.1016/j.rser.2019.01.007.

[5] Adeyanju, E., Okeke, C.A., 2019. Exposure effect to cement dust pollution: a mini review. SN Appl Sci 1, 1572. https://doi.org/10.1007/s42452-019-1583-0.

[6] Dimkpa, C.O., McLean, J.E., Martineau, N., Britt, D.W., Haverkamp, R., Anderson, A.J., 2013. Silver nanoparticles disrupt wheat (*Triticum aestivum* L.) Growth in a Sand Matrix. Environ Sci Technol 47, 1082–1090. https://doi.org/10.1021/es302973y.

[7] Brown, D.M., Donaldson, K., Borm, P.J., Schins, R.P., Dehnhardt, M., Gilmour, P., Jimenez, L.A., Stone, V., 2004. Calcium and ROS-mediated activation of transcription factors and TNF-α cytokine gene expression in macrophages exposed to ultrafine particles. Am J Physiol Lung Cell Mol Physiol 286, L344–L353. https://doi.org/10.1152/ajplung.00139.2003.

[8] Buzea, C., Pacheco, I.I., Robbie, K., 2007. Nanomaterials and nanoparticles: sources and toxicity. Biointerphases 2, MR17–MR71. https://doi.org/10.1116/1.2815690.

[9] Medici, S., Peana, M., Pelucelli, A., Zoroddu, M.A., 2021. An updated overview on metal nanoparticles toxicity. Semin Cancer Biol 76, 17–26. https://doi.org/10.1016/j.semcancer.2021.06.020.

[10] Kumar, P., Robins, A., Vardoulakis, S., Britter, R., 2010. A review of the characteristics of nanoparticles in the urban atmosphere and the prospects for developing regulatory controls. Atmos Environ 44, 5035–5052. https://doi.org/10.1016/j.atmosenv.2010.08.016.

[11] Commodore, S., Christopher, S., Wolf, B., Svendsen, E., 2023. Assessment of trace elements directly from archived total suspended particulate filters by laser ablation ICP-MS: a case study of South Carolina. J Trace Elem Miner 3, 100041. https://doi.org/10.1016/j.jtemin.2022.100041.

[12] Scherer, C., Noskov, S., Utech, S., Bantz, C., Mueller, W., Krohne, K., Maskos, M., 2010. Characterization of polymer nanoparticles by asymmetrical flow field flow fractionation (AF-FFF). J Nanosci Nanotechnol 10, 6834–6839. https://doi.org/10.1166/jnn.2010.2973.

[13] Souza, T.G.F., Ciminelli, V.S.T., Mohallem, N.D.S., 2016. A comparison of TEM and DLS methods to characterize size distribution of ceramic nanoparticles. J Phys Conf Ser 733, 012039. https://doi.org/10.1088/1742-6596/733/1/012039.

[14] Chicea, D., 2010. Nanoparticles and nanoparticle aggregates sizing by DLS and AFM. Optoelectron Adv Mater 4, 1310–1315.

[15] Rades, S., Hodoroaba, V.-D., Salge, T., Wirth, T., Lobera, M.P., Labrador, R.H., Natte, K., Behnke, T., Gross, T., Unger, W.E.S., 2014. High-resolution imaging with SEM/T-SEM, EDX and SAM as a combined methodical approach for morphological and elemental analyses of single engineered nanoparticles. RSC Adv 4, 49577–49587. https://doi.org/10.1039/C4RA05092D.

[16] Pace, H.E., Rogers, N.J., Jarolimek, C., Coleman, V.A., Higgins, C.P., Ranville, J.F., 2011. Determining transport efficiency for the purpose of counting and sizing nanoparticles via single particle inductively coupled plasma mass spectrometry. Anal Chem 83, 9361–9369. https://doi.org/10.1021/ac201952t.

[17] Azimzada, A., Jreije, I., Hadioui, M., Shaw, P., Farner, J.M., Wilkinson, K.J., 2021. Quantification and characterization of Ti-, Ce-, and Ag-nanoparticles in global surface waters and precipitation. Environ Sci Technol 55, 9836–9844. https://doi.org/10.1021/acs.est.1c00488.

[18] Gondikas, A.P., Kammer, F.V.D., Reed, R.B., Wagner, S., Ranville, J.F., Hofmann, T., 2014. Release of TiO_2 nanoparticles from sunscreens into surface waters: a one-year survey at the Old Danube Recreational Lake. Environ Sci Technol 48, 5415–5422. https://doi.org/10.1021/es405596y.

[19] Wang, J.-L., Alasonati, E., Tharaud, M., Gelabert, A., Fisicaro, P., Benedetti, M.F., 2020. Flow and fate of silver nanoparticles in small French catchments under different land-uses: the first one-year study. Water Res 176, 115722. https://doi.org/10.1016/j.watres.2020.115722.

[20] Gelin, M., Tharaud, M., Benedetti, M.F., 2025. Volcanic aerosols captured by plants: a study of nanoparticles and their chemical composition. Sci Total Environ 963, 178505. https://doi.org/10.1016/j.scitotenv.2025.178505.

[21] Avramescu, M.-L., Casey, K., Levesque, C., Chen, J., Wiseman, C., Beauchemin, S., 2024. Identification and quantification of trace metal(loid)s in water-extractable road dust nanoparticles using SP-ICP-MS. Sci Total Environ 924, 171720. https://doi.org/10.1016/j.scitotenv.2024.171720.

[22] Badamasi, H., 2017. Biomonitoring of air pollution using plants. MAYFEB J Environ Sci 2, 14.

[23] Chrabąszcz, M., Mróz, L., 2017. Tree Bark, a valuable source of informationon air quality. Pol J Environ Stud 26, 453–466. https://doi.org/10.15244/pjoes/65908.

[24] Catinon, M., Ayrault, S., Spadini, L., Boudouma, O., Asta, J., Tissut, M., Ravanel, P., 2011. Tree bark suber-included particles: a long-term accumulation site for elements of atmospheric origin. Atmos Environ 45, 1102–1109. https://doi.org/10.1016/j.atmosenv.2010.11.038.

[25] Škrbić, B., Milovac, S., Matavulj, M., 2012. Multielement profiles of soil, road dust, tree bark and wood-rotten fungi collected at various distances from high-frequency road in urban area. Ecol Indic 13, 168–177. https://doi.org/10.1016/j.ecolind.2011.05.023.

[26] Olajire, A.A., Ayodele, E.T., 2003. Study of atmospheric pollution levels by trace elements analysis of tree bark and leaves. Bull Chem Soc Ethiop 17. https://doi.org/10.4314/bcse.v17i1.61724.

[27] Carvallo, C., Isambert, A., Franke, C., Turcati, L., Sivry, Y., Coural, S., Macouin, M., Rousse, S., Fluteau, F., 2024. Ecorc'Air: a citizen science project for the biomonitoring of vehicular air pollution in Paris, France. Community Sci 3, e2024CSJ000084. https://doi.org/10.1029/2024CSJ000084.

[28] Leite, A.D.S., Rousse, S., Léon, J. -F., Trindade, R.I.F., Haoues-Jouve, S., Carvallo, C., Dias-Alves, M., Proietti, A., Nardin, E., Macouin, M., 2022. Barking up the right tree: using tree bark to track airborne particles in school environment and link science to society. GeoHealth 6, e2022GH000633. https://doi.org/10.1029/2022GH000633.

[29] Rowell, R.M. (Ed.), 2012. Handbook of Wood Chemistry and Wood Composites, 0 ed. CRC Press. https://doi.org/10.1201/b12487.

[30] Ayrault, S., El Alaoui-Faris, F.E., Asta, J., Tissut, M., Daudin, L., Mariet, C., Ravanel, P., Gaudry, A., Cherkaoui, R., 2007. A PIXE and ICP-MS analysis of metallic atmospheric contaminants in tree bark tissues, a basis for biomonitoring uses*. J Toxicol Environ Health A 70, 742–749. https://doi.org/10.1080/15287390701236397.

[31] Deng, Y., Zhao, R., 2015. Advanced Oxidation Processes (AOPs) in wastewater treatment. Curr Pollut Rep 1, 167–176 (vil.).

[32] Vilhunen, S., Sillanpää, M., 2010. Recent developments in photochemical and chemical AOPs in water treatment: a mini-review. Rev Environ Sci Biotechnol 9, 323–330. https://doi.org/10.1007/s11157-010-9216-5.

[33] Clark, N.J., Clough, R., Boyle, D., Handy, R.D., 2019. Development of a suitable detection method for silver nanoparticles in fish tissue using single particle ICP-MS. Environ Sci Nano 6, 3388–3400. https://doi.org/10.1039/C9EN00547A.

[34] Campos, N., De Oliveira, M., Izumi, C., De Sousa, R., 2017. Alkaline solubilization of chicken tissues monitored by Raman Spectroscopy followed by Pb determination by GF AAS. J Braz Chem Soc. https://doi.org/10.21577/0103-5053.20170148.

[35] Cerqueira, U.M.F.M., Alves, J.P.S., Santos, W.N.L., Da Silva Pita, B., Novaes, C.G., Araújo, S.A., Bezerra, M.A., 2024. Recent applications of tetramethylammonium hydroxide (TMAH) in the sample preparation for elemental analysis by spectroanalytical techniques. Adv Sample Prep 9, 100104. https://doi.org/10.1016/j.sampre.2024.100104.

[36] Calvimontes, A., Mauersberger, P., Nitschke, M., Dutschk, V., Simon, F., 2011. Effects of oxygen plasma on cellulose surface. Cellulose 18, 803–809. https://doi.org/10.1007/s10570-011-9511-5.
[37] Kh Elnagar, R.S. Abouelella, A.M. Abdel-Razik, O. Abdel-Kareem, Evaluating new ageing technique for archaeological textile conservation field using raduifrequency air and oxygen plasma, (2022). https://doi.org/10.5281/ZENODO.7306067.
[38] Sahin, H.T., 2009. RF-O2 plasma surface modification of kraft lignin derived from wood pulping. WOOD Res 54.
[39] Tharaud, M., Louvat, P., Benedetti, M.F., 2021. Detection of nanoparticles by single-particle ICP-MS with complete transport efficiency through direct nebulization at few-microlitres-per-minute uptake rates. Anal Bioanal Chem 413, 923–933. https://doi.org/10.1007/s00216-020-03048-y.
[40] M. Tharaud, Vers une version 2.0 de la spICPMS pour mieux comprendre la biogéochimie des nanophases dans l'environnement., 2022.
[41] Catinon, M., Ayrault, S., Daudin, L., Sevin, L., Asta, J., Tissut, M., Ravanel, P., 2008. Atmospheric inorganic contaminants and their distribution inside stem tissues of Fraxinus excelsior L. Atmos Environ 42, 1223–1238. https://doi.org/10.1016/j.atmosenv.2007.10.082.
[42] Jablonský, M., Iš, J.K., Ház, A., Šima, J., 2013. Characterization and comparison by UV spectroscopy of precipitated lignins and commercial lignosulfonates. Cellul Chem Technol.
[43] Abdelaziz, O.Y., Hulteberg, C.P., 2017. Physicochemical characterisation of technical lignins for their potential valorisation. Waste Biomass Valoriz 8, 859–869. https://doi.org/10.1007/s12649-016-9643-9.
[44] Lee, R.A., Bédard, C., Berberi, V., Beauchet, R., Lavoie, J.-M., 2013. UV–Vis as quantification tool for solubilized lignin following a single-shot steam process. Bioresour Technol 144, 658–663. https://doi.org/10.1016/j.biortech.2013.06.045.
[45] Derkacheva, O., Sukhov, D., 2008. Investigation of lignins by FTIR spectroscopy. Macromol Symp 265, 61–68. https://doi.org/10.1002/masy.200850507.
[46] Reyes-Rivera, J., Terrazas, T., 2017. Lignin Analysis by HPLC and FTIR. In: De Lucas, M., Etchhells, J.P. (Eds.), Xylem. Springer New York, New York, NY, pp. 193–211. https://doi.org/10.1007/978-1-4939-6722-3_14.
[47] Wang, Z., Zhang, L., Zhao, J., Xing, B., 2016. Environmental processes and toxicity of metallic nanoparticles in aquatic systems as affected by natural organic matter. Environ Sci Nano 3, 240–255. https://doi.org/10.1039/C5EN00230C.
[48] Riedel, S., Kaupp, M., 2009. The highest oxidation states of the transition metal elements. Coord Chem Rev 253, 606–624. https://doi.org/10.1016/j.ccr.2008.07.014.
[49] deB Darwent, B., 1970. Bond dissociation energies in simple molecules. National Bureau of Standards, Washington, D.C.
[50] Vindedahl, A.M., Strehlau, J.H., Arnold, W.A., Penn, R.L., 2016. Organic matter and iron oxide nanoparticles: aggregation, interactions, and reactivity. Environ Sci Nano 3, 494–505. https://doi.org/10.1039/C5EN00215J.
[51] Turan, N.B., Erkan, H.S., Engin, G.O., Bilgili, M.S., 2019. Nanoparticles in the aquatic environment: Usage, properties, transformation and toxicity—A review. Process Saf Environ Prot 130, 238–249. https://doi.org/10.1016/j.psep.2019.08.014.
[52] Tso, C., Zhung, C., Shih, Y., Tseng, Y.-M., Wu, S., Doong, R., 2010. Stability of metal oxide nanoparticles in aqueous solutions. Water Sci Technol 61, 127–133. https://doi.org/10.2166/wst.2010.787.
[53] U. Schwertmann, Solubility and dissolution of iron oxides, (1991).
[54] Ghulam, M., Hajira, T., Muhammad, S., Nasir, A., 2013. Synthesis and characterization of cupric oxide (CuO) nanoparticles and their application for the removal of dyes. Afr J Biotechnol 12, 6650–6660. https://doi.org/10.5897/AJB2013.13058.
[55] Sousa, V.S., Teixeira, M.R., 2013. Aggregation kinetics and surface charge of CuO nanoparticles: the influence of pH, ionic strength and humic acids. Environ Chem 10, 313. https://doi.org/10.1071/EN13001.
[56] Jurašin, D.D., Ćurlin, M., Capjak, I., Crnković, T., Lovrić, M., Babič, M., Horák, D., Vinković Vrček, I., Gajović, S., 2016. Surface coating affects behavior of metallic nanoparticles in a biological environment. Beilstein J Nanotechnol 7, 246–262. https://doi.org/10.3762/bjnano.7.23.
[57] Liu, J., Louie, S.M., Zhao, J., Gao, X., Hu, Y., 2022. Aggregation of varied organic coated magnetite nanoparticles: Adsorbed mass and thickness of coatings and interactions with natural organic matter. Sci Total Environ 831, 154976. https://doi.org/10.1016/j.scitotenv.2022.154976.
[58] Lučić, M., Ščančar, R.M., Ščančar, J., Fiket, Ž., Arah, B., Vidmar, J., 2025. Optimized extraction, quantification and characterization of seven environmentally relevant metallic nanoparticles in sewage sludge: Occurrence, composition and environmental risk assessment. J Hazard Mater 497, 139734. https://doi.org/10.1016/j.jhazmat.2025.139734.
[59] Conway, J.R., Adeleye, A.S., Gardea-Torresdey, J., Keller, A.A., 2015. Aggregation, dissolution, and transformation of copper nanoparticles in natural waters. Environ Sci Technol 49, 2749–2756. https://doi.org/10.1021/es504918q.